Provided for non-commercial research and education use.
Not for reproduction, distribution or commercial use.

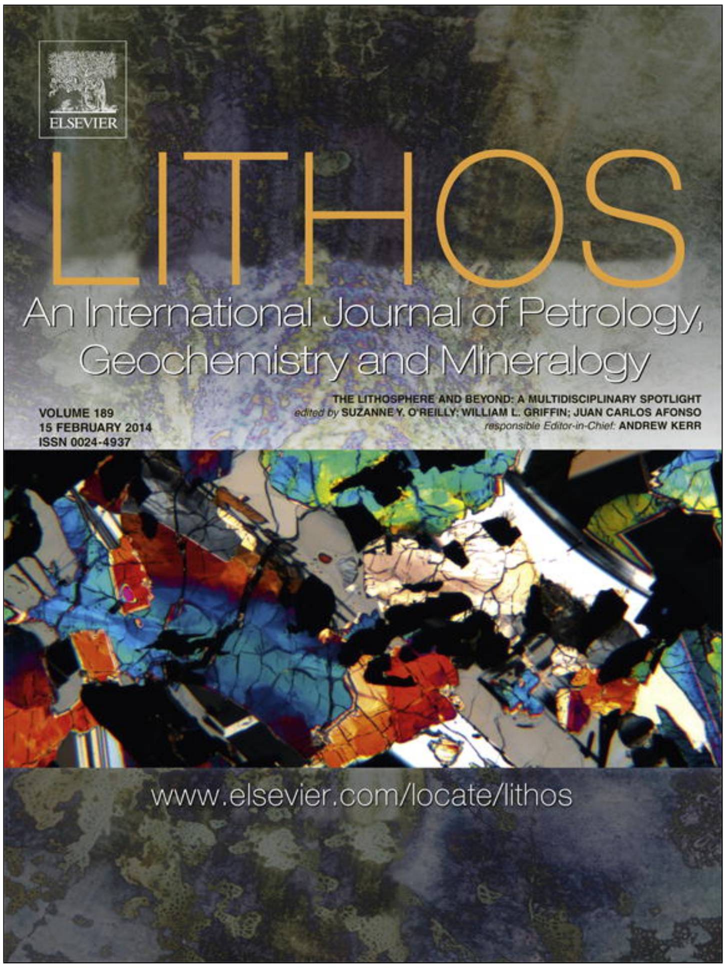

This article appeared in a journal published by Elsevier. The attached copy is furnished to the author for internal non-commercial research and education use, including for instruction at the authors institution and sharing with colleagues.

Other uses, including reproduction and distribution, or selling or licensing copies, or posting to personal, institutional or third party websites are prohibited.

In most cases authors are permitted to post their version of the article (e.g. in Word or Tex form) to their personal website or institutional repository. Authors requiring further information regarding Elsevier's archiving and manuscript policies are encouraged to visit:

http://www.elsevier.com/authorsrights

Author's personal copy

Lithos 189 (2014) 77–88

Contents lists available at ScienceDirect

Lithos

journal homepage: www.elsevier.com/locate/lithos

Lateral migration of a foundering high-density root: Insights from numerical modeling applied to the southern Sierra Nevada

J.L. Valera [a], A.M. Negredo [a,b], M.I. Billen [c,*], I. Jiménez-Munt [d]

[a] Dept. of Geophysics, Faculty of Physics, Universidad Complutense de Madrid, Plaza de Ciencias, 1, 28040 Madrid, Spain
[b] Instituto de Geociencias (CSIC-UCM), Faculty of Physics, Universidad Complutense de Madrid, Plaza de Ciencias, 1, 28040 Madrid, Spain
[c] Department of Geology University of California, Davis, Davis, CA 95616, USA
[d] Instituto de Ciencias de la Tierra 'Jaume Almera', CSIC, C/Sole i Sabaris s/n., 08028 Barcelona, Spain

ARTICLE INFO

Article history:
Received 12 March 2013
Accepted 27 August 2013
Available online 3 September 2013

Keywords:
Thermo-mechanical modeling
Delamination
Dynamic topography
Isostatic topography
Comparison to seismic observations
Southern Sierra Nevada

ABSTRACT

The southern Sierra Nevada is a geodynamically complex region where several models have been proposed to explain the rapid removal of lithospheric mantle occurring sometime between 8.0 and 3.5 Ma. Tomographic studies show the presence of an east-dipping slab-shaped fast seismic anomaly reaching to about 300 km depth below the western Sierras and Great Valley, and receiver function studies indicate a broad region of lithosphere removal. This work presents thermo-mechanical modeling of asymmetric foundering of a high-density batholithic root with lateral intrusion of asthenospheric material. The predicted evolution is controlled by: a) the upwelling of buoyant asthenosphere facilitated by the presence of a weakened lithospheric mantle adjacent to a dense batholitic root, b) the westward inflow enabled by a low viscosity lower crust, and c) negative buoyancy of a batholithic dense root. The dynamics of these models can be characterized as a slowly migrating lithosphere foundering process driven by the density anomaly of the ultramafic root, but controlled by the magnitude of the lower crustal viscosity, which determines the rate at which asthenospheric material can flow into the opening lower crustal gap. Final model-predicted upper-mantle structure is compatible with existing tomographic images and the observed V-shape geometry of the Moho below the western margin of the southern Sierra Nevada. Model-predicted topography is also generally consistent with observations, and shows a monotonous uplift of the high region since 7 Ma and presently ongoing, and an area of maximum subsidence west of the area of the V-shaped Moho, due to the pull exerted by the sinking of the high-density root.

© 2013 Elsevier B.V. All rights reserved.

1. Introduction

The Sierra Nevada Mountain Range of California is one of the highest (about 3 km mean elevation) in the United States (Fig. 1); however, seismic refraction studies (Fliedner et al., 2000) and analyses of receiver functions (Frassetto et al., 2011; Gilbert et al., 2007; Zandt et al., 2004) have confirmed previous studies suggesting that the crust beneath the south and central range is only 35–40 km thick (Jones et al., 1994; Ruppert et al., 1998; Wernicke et al., 1996), contrary to expectations from isostasy of thick crust supporting regions of high elevation.

1.1. History and current observations

The rocks exposed in the Sierra Nevada are the batholith associated with subduction related arcs that were active 160–150 Ma and 100–85 Ma, and became inactive during flat-slab subduction associated with the Laramide (Ducea, 2001). Normal subduction likely resumed for a short period around 18 Ma before the Mendocino Triple Junction migrated northward past the latitude of the southern Sierra Nevada at 20–15 Ma and cleared the central Sierra Nevada at about 5 Ma (Atwater and Stock, 1998). The southern edge of the Juan de Fuca slab is currently located just north of Lake Tahoe (39°N, Fig. 1) as demonstrated by recent tomographic studies (Schmandt and Humphreys, 2010).

Petrologic studies indicate that a large amount of material from the mantle lithosphere was removed from beneath the southern Sierra Nevada sometime between 8.0 and 3.5 Ma. The presence of a 40–60 km thick eclogite-rich layer in the crust beneath the Sierran granitoid batholith before about 8 Ma has been inferred from examination of entrained xenoliths originating between depths of 40 and >100 km (Ducea and Saleeby, 1996, 1998a; Lee et al., 2000, 2001). This dense eclogite-rich layer constituted the batholithic root, a thick sequence of mafic–ultramafic, mainly eclogite-facies cumulates and residues that formed during generation of the Mesozoic Sierra Nevada Batholith (Ducea and Saleeby, 1998a). Basaltic magmatism and new spinel peridotite xenoliths erupted at 3.5 Ma,

* Corresponding author.
E-mail address: mibillen@ucdavis.edu (M.I. Billen).

0024-4937/$ – see front matter © 2013 Elsevier B.V. All rights reserved.
http://dx.doi.org/10.1016/j.lithos.2013.08.021

Author's personal copy

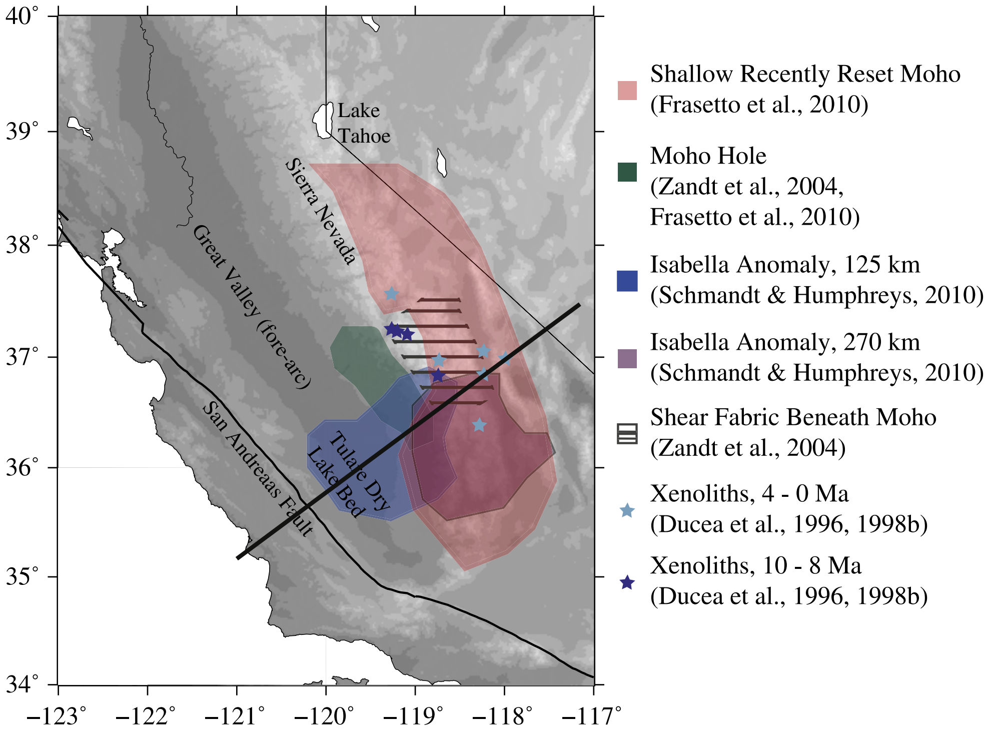

Fig. 1. Summary map of observations. Gray scale image is topography indicating the location of the uplifted Sierra Nevada adjacent to the Great Valley fore-arc basin. Colored shaded regions indicate seismic observations as listed in the legend. Stars indicate locations of xenolith data constraining the timing of the batholithic root loss. Southwest to northeast line indicates approximate orientation of two-dimensional profile used in model simulations.

implying the absence of the eclogite layer and presumably its removal, together with the deeper lithospheric mantle, by this time (Farmer et al., 2002).

Seismic observations also support the conclusion that a portion of the lower crust and mantle lithosphere has been removed beneath the southern Sierra Nevada. According to recent tomographic work, the "Isabella Anomaly", a southeast-dipping high velocity anomaly that extends to about 300 km in depth beneath the western Sierras and Great Valley (Boyd et al., 2004; Schmandt and Humphreys, 2010), is the removed material descending into the mantle (see outlines of high seismic velocity body in Fig. 1). A second high velocity anomaly exists to the north (39–40°N), but could be associated with continued subduction of the southern edge of the Juan de Fuca plate.

Receiver function studies also indicate an anomalously shallow (30–40 km) and strong Moho reflector extending from 35 to 39°N, mainly beneath the eastern Sierra Nevada, except where it extends west below the Isabella Anomaly where it reaches depths of 50 km (Frassetto et al., 2011; Zandt et al., 2004). This region is coincident with the region of inferred lithosphere removal based on xenolith data and also has higher heat flow than the regions beneath the western Sierra Nevada (Frassetto et al., 2011). The Moho reflector is deflected downward into a V-shape cone above the Isabella Anomaly with a gap at its apex ("Moho-hole") caused by wave scattering (Gilbert et al., 2007; Zandt et al., 2004): a similar structure is also observed at about 38°N in the central Sierra Nevada and has been interpreted as a region of incipient lithosphere removal (Frassetto et al., 2011).

Removal of the lower crust and mantle–lithosphere should also manifest in vertical motion of the crust as it re-adjusts isostatically. Using geomorphology and thermochronometry, Clark et al. (2005) proposed two fast uplift phases since 32 Ma in the southern Sierra: a first phase at some time between 32 and 3.5 Ma and a second phase from 3.5 Ma to present. Although the discussion about the topographic history of southern Sierra Nevada is still ongoing (see, for instance, Figueroa and Knott, 2010; Henry, 2009; Mahéo et al., 2009; Stock et al., 2005) it has been proposed that the first phase of uplift is related to delamination or dripping, whereas the second phase is likely due to flexural response of the residual lithosphere to the progressive reduction of its equivalent elastic thickness (Bennett et al., 2009). In addition, fossil records from basins just east of the current Sierra Nevada near Reno indicate a lack of paleo-relief prior to about 2.6 Ma in the north-central part of the range (Trexler et al., 2012), indicating that neither phase of uplift reach this far north until after 2.6 Ma.

Both phases should accommodate a total topographic increase of about 2.5 km since the Late Cretaceous (Clark et al., 2005). Stratigraphic evidence for late Cenozoic tilting of the western Sierra also suggests up to 2.0 km of uplift associated with the second episode of uplift. Continuous GPS measurements of relative vertical crustal motion (Bennett et al., 2009) indicate that topographic relief is presently increasing along the southeastern flank of the Sierra Nevada range.

1.2. Previous geodynamical models

Removal of continental lithosphere has been proposed in mountain ranges to explain a wide range of observations such as lithospheric thinning, anomalously high heat flow, regional uplift, change of stress field toward extension, the presence of high seismic velocity anomalies in the upper mantle far from present subduction zones, and change in the composition of erupted magmas. The presence of one or more of these observations has led to claims of lithospheric removal below the Sierra Nevada mountains (Ducea and Saleeby, 1998a,b; Harig et al., 2008; Le Pourhiet et al., 2006; Saleeby et al., 2003; Zandt et al., 2004), the Colorado plateau (Bird, 1979; Levander et al., 2011), the Altiplano-Puna region (Beck and Zandt, 2002; Kay and Kay, 1993; Molnar and Garzione, 2007), the Alboran sea (Calvert et al., 2000; Duggen et al., 2003; Platt and Vissers, 1989; Seber et al., 1996; Valera et al., 2008; Vissers, 2012), the Apennines (Channel and Mareschal, 1989; Faccenda et al., 2009), the Carpathian–Pannonian area (Fillerup et al., 2010; Gemmer and Houseman, 2007; Knapp et al., 2005; Lorinczi and

Author's personal copy

Houseman, 2009), the Rwenzori Mountains in the East African Rift System (Wallner and Schmeling, 2010), Eastern Anatolia (Göğüş and Pysklywec, 2008b), the Tibetan plateau (Bird, 1978; England and Houseman, 1989; Houseman et al., 1981; Jiménez-Munt and Platt, 2006; Tilmann et al., 2003), New Zealand (Furlong and Kamp, 2009; Stern et al., 2006) among many other areas. However, none of these regions share the previous history of flat-slab subduction followed by opening of a slab window as found in the southern Sierra Nevada region.

The processes responsible for removal of continental lithospheric mantle are still under debate, but most of the related models presented during the last 30 years can be grouped into two categories: those based on viscous convective removal (Rayleigh–Taylor instability) (e.g., Elkins-Tanton, 2007; England and Houseman, 1989; Harig et al., 2008; Houseman and Molnar, 2001; Houseman et al., 1981; Lorinczi and Houseman, 2009; Marotta et al., 1998; Molnar and Jones, 2004; West et al., 2009) and those based on lithospheric delamination (e.g., Bajolet et al., 2012; Bird, 1978, 1979; Bird and Baumgardner, 1981; Göğüş and Pysklywec, 2008a,b; Göğüş et al., 2011; Morency and Doin, 2004; Schott and Schmeling, 1998). In the case of a Rayleigh–Taylor instability an initial density perturbation grows due to lateral flow and thinning of the dense layer, whereas in the case of delamination sinking of the dense layer is accomplished by separation from the layer above and flow of buoyant material between the layers.

Several numerical studies explain the lithospheric mantle removal beneath the Sierra Nevada Mountains by the development of two symmetric Rayleigh–Taylor instabilities propagating northward and southward, with two high seismic velocity anomalies located to the north and to the south of the Central Valley, representing the present-day position of the lithospheric downwellings imaged seismically (e.g., Harig et al., 2008; Molnar and Jones, 2004). However, it has been pointed out that the observations associated with these two anomalies, and therefore their inferred evolution, are not the same (Harig et al., 2008), which poses some difficulties in assigning both anomalies to the same process. In addition, the northern anomaly is near the current edge of the subducting Juan de Fuca slab, and therefore may be associated with flow around the slab edge rather than destabilization of the batholithic root.

Combining the existing geological constraints with data obtained from receiver function seismology, Zandt et al. (2004) proposed the following sequential history for the evolution of the southern Sierra Nevada, based on the lateral propagation of the foundering of an ultramafic root. First, the northward migration of the Mendocino triple junction passed through this region between 20 and 15 Ma, exposing the Sierran lithosphere to the asthenosphere of the 'slab window' (e.g., Atwater and Stock, 1998). Second, the dense lithospheric root became unstable through a Rayleigh–Taylor mechanism. Finally, as the instability grew, a pronounced asymmetry in the foundering developed, producing the lateral migration of the Rayleigh–Taylor instability, accompanied by a more widespread mantle upwelling under the western Basin and Range and easternmost Sierra.

However, other seismic observations reveal that the fast seismic anomaly imaged in the Zandt et al. (2004) study has two compositional layers, with values consistent with iron-rich eclogite overlying (to the east) of a magnesium–garnet rich layer (Boyd et al., 2004). This compositional layering suggests that the descending lithosphere preserves its original layered structure. In addition, the eastward dip indicates that material moved somewhat to the east relative to the overlying crust (Boyd et al., 2004). This eastward dip is suggested to be inconsistent with the structures predicted by the Rayleigh–Taylor based models (Boyd et al., 2004). Furthermore, it has been argued (Le Pourhiet et al., 2006) that the characteristic time-scale of the Rayleigh–Taylor instability is intrinsically longer than that inferred from observations in this region, and that instead the Stokes sinking velocity determines the sinking rate of the batholithic root. However, for a given wavelength of the initial perturbation, it is possible to develop Rayleigh–Taylor instabilities more rapidly with non-Newtonian rheology because the viscous resistance to sinking decreases as the instability grows (Molnar and Jones, 2004). Regardless of the rheology, Rayleigh–Taylor instabilities are limited in the thickness of lithospheric material that is entrained (e.g., Göğüş and Pysklywec, 2008a): the approximately 100 km wide diameter of the Isabella Anomaly would require lateral flow of a 50–100 km thick layer making it difficult to explain the downwelling with this mechanism unless the entire lithosphere can be entrained (i.e., has a low viscosity).

Le Pourhiet et al. (2006) proposed an alternative delamination model for the recent evolution of the southern Sierra Nevada, in which a small-scale instability induces localized convection that thermally erodes the lithospheric-mantle and creates a low viscosity zone connecting the asthenosphere with the lower crust. In this model, a long phase of strain localization induced by imposed extension, lithospheric break-off and asthenospheric spreading along the Moho, is followed by a period of lithospheric mantle delamination from 6 to 2 Ma and root removal from 2 Ma to present. The removed root forms an elongated east-dipping high-density body shifted westward from the region of initial lithospheric delamination. This delamination model reproduces some of the observations, including the downwelling shifted westward of the Sierra Nevada, and general characteristics of the topography.

A third explanation for the lithospheric downwelling in the southern Sierra Nevada is foundering of a stalled portion of the Juan de Fuca plate (Bohannon and Parsons, 1995; Forsyth and Rau, 2009). However, several lines of evidence argue against this interpretation: the required geometry of the dipping slab at the time of lithospheric removal beneath the Sierra Nevada, the lack of a strong seismic reflector expected for the structural boundary at the top of the stalled slab surface (Frassetto et al., 2011), and the rapid time-scale (<4.5–14.5 My) of detachment and sinking for young, stalled lithosphere (Andrews and Billen, 2009).

The purpose of this study is to test the viscosity and density structure that controls the mode of asymmetric lithospheric foundering inferred for the southern Sierra Nevada, and specifically to test the hypothesis that weakening of the mantle lithosphere destabilized the dense batholithic root creating an east-dipping slab-shaped structure. In order to specifically test the dynamic effects of different parts of the crust–lithosphere structure, we adopt a Newtonian (linear) viscosity, but choose viscosity values consistent with a non-Newtonian rheology at the appropriate strain-rates. Therefore the viscosity values cited here should be treated as effective viscosities (i.e., low values correspond to regions deforming at high strain-rates). In addition, while many models of delamination assume either a state of regional compression or extension (see references above), we do not impose any regional strain. Most of the model results shown here fall into the category of slowly migrating delamination but are initiated by a compositional density anomaly. In addition, small changes in the viscosity of key structures in the crust or mantle shift the dynamics into that of a more slowly evolving Rayleigh–Taylor instability.

2. Numerical modeling

We present 2D numerical models using TEMESCH (TEmperature and Motion Equation SCHeme), a MATLAB finite difference code developed by the authors (Valera, 2009; Valera et al., 2008, 2011), which solves the equations of conservation of mass, momentum and energy for an incompressible fluid. Density variations have been neglected in the motion equation except when they are coupled to the gravitational acceleration in the buoyancy force term (left hand side of Eq. (1)). Inertial forces are neglected. The thermal effects of radiogenic heat production and adiabatic heating (second and third terms on the right side of Eq. (2)) are included in the energy equation (e.g., Ita and King, 1994; Schmeling, 1989; Tritton, 1988), whereas shear heating is neglected. The final equations are:

$$\frac{\partial}{\partial x}(\rho g) = 4\frac{\partial^2}{\partial x \partial z}\left(\mu \frac{\partial^2}{\partial x \partial z}\Psi\right) + \left(\frac{\partial^2}{\partial z^2} - \frac{\partial^2}{\partial x^2}\right)\mu\left(\frac{\partial^2}{\partial z^2} - \frac{\partial^2}{\partial x^2}\right)\Psi \qquad (1)$$

Author's personal copy

$$\frac{\partial T}{\partial t}+u_x\frac{\partial T}{\partial x}+u_z\frac{\partial T}{\partial z}=\frac{k}{\rho c_p}\left(\frac{\partial^2 T}{\partial x^2}+\frac{\partial^2 T}{\partial z^2}\right)+\frac{H}{c_p}+u_z\frac{\alpha g}{c_p}T \tag{2}$$

where x is the horizontal coordinate; ρ is the density; g is the acceleration of gravity; z is the vertical coordinate, pointing downward; μ is the dynamic viscosity; T is the temperature; t is the time; H is the radiogenic heat production; c_p is the specific heat; k is the thermal conductivity; α is the thermal expansion coefficient; u_k is the k-component of the velocity vector. The velocity is related to the stream function, Ψ, as:

$$u_x=\frac{\partial\Psi}{\partial z};\quad u_z=-\frac{\partial\Psi}{\partial x}. \tag{3}$$

The values of the parameters used are listed in Table 1. Note this form of the equations is derived from the extended Boussinesq Approximation, which is incompressible, but includes both adiabatic heating and shear heating (Schubert et al., 2001): instead of using the Boussinesq Approximation the adiabatic heating term is kept in order to stabilize the numerical solution, while the shear heating term is neglected in order to avoid numerical temperature instabilities. The reader is referred to Valera et al. (2008) for a detailed explanation of derivation of Eqs. (1) and (2) from the primitive forms of momentum and energy equations.

The TEMESCH code uses a second order, central ADI (Alternating Difference Implicit) scheme combined with the Thomas Algorithm to solve the thermal equation (see Negredo et al., 2004 for further details); and a second order, central finite difference scheme for solving the motion equation. Free slip boundary conditions are applied at all boundaries, and therefore the models develop in the absence of imposed extension. The surface temperature is fixed at 0 °C and the side boundaries have zero horizontal heat flow (Fig. 2a). In order to maintain a constant geothermal gradient in the mantle throughout the simulation a constant heat flow computed from the initial geotherm is applied at the bottom.

The TEMESCH code uses two different grids: an Eulerian grid with fixed nodes and a Lagrangian grid with moving markers carrying the material properties. The Eulerian grid is a Cartesian box with a resolution of 121 × 80 nodes in the x- and z-directions. The size of the modeled domain is 600 × 400 km. A time-step of 0.1 My is used. The Lagrangian grid has three times more markers than nodes in each direction. Properties (density and viscosity) are computed at each node as an arithmetic mean of values at the nearest markers. Use of the arithmetic mean for the viscosity rather than the geometric mean leads to higher averaged viscosity values, which in turn could lead to slower rates of deformation (Schmeling et al., 2008). This effect is small where viscosity is controlled by smooth temperature gradients, but could lead to differences in viscosity of an order of magnitude where viscosity jumps at compositional boundaries. Therefore, the rates of deformation presented here are conservative. Convergence of the results has been checked by varying the spatial and time resolution and requiring that the Courant criterion (e.g., Anderson, 1995) is attained for all simulations (see Valera, 2009; Valera et al., 2008 for further details and benchmarks).

Table 1
Fixed parameters used in the modeling.

Symbol	Meaning	Value
g	Gravity acceleration	$9.8\ m\ s^{-2}$
c_p	Specific heat	$1.3\times10^3\ J\ C^{-1}\ kg^{-1}$
α	Thermal expansion coefficient	$3.7\times10^{-5}\ C^{-1}$
k	Thermal conductivity	$3.2\ W\ m^{-1}\ C^{-1}$
–	Horizontal extent	600 km
–	Vertical extent	400 km
Q_b	Basal heat flow	$1.3\ mW\ m^{-2}$
H_{uc}	Radiogenic heat production for the upper crust	$1.5\times10^{-6}\ W\ m^{-3}$
H_{gb}	Radiogenic heat production for the granitic batholith	$1.5\times10^{-6}\ W\ m^{-3}$
H_{lc}	Radiogenic heat production for the lower crust	$0.2\times10^{-6}\ W\ m^{-3}$
T_o	Temperature at the base of the lithosphere	1300 °C
b	Parameter in viscous law (see Eq. (4))	15

The modeled section is a generic profile across the southern Sierra Nevada Mountains after the passage of the slab window and oriented roughly northeast to southwest (Fig. 2a). Therefore, the lithosphere structure in the western part of the model (Great Valley) corresponds to a fore arc basin with a single crustal layer overlying a mantle–lithosphere layer, whereas the central and eastern parts of the model correspond to lithosphere of continental affinity with both upper and lower crust, and a thicker lithosphere. The two regions are merged with a sloped lithosphere boundary and pinching out of the lower crust just west of the batholith (Fig. 2a). To the right (east) of the batholithic root a 100-km-wide region of low viscosity lithospheric mantle is introduced to simulate a lithosphere weakened by water migrating up from the dehydrating slab during the previous subduction of the Farallon Plate. Because of flat slab subduction, this weak region and the batholith would have been insulated from the mantle by the flat slab until it steepened before opening of the slab window in the late Cenozoic.

The initial model state considered in our models is significantly different from that proposed by Le Pourhiet et al. (2006), who assumed a homogeneous lithospheric thickness and a semi-circular perturbation representing the batholithic root. They did not include any region of hydrated (weak) lithospheric mantle, but instead produced a weakened lithospheric mantle by the localization of strain caused by applied extension. In contrast, the initial state modeled here is more similar to the setup imposed in the generic delamination modeling by Göğüş and Pysklywec (2008a). These authors used a homogeneously thick lithospheric mantle, including a denser zone and an adjacent low viscosity zone, with a horizontal weak channel along the base of the crust. We prefer this setup because it better represents the scenario proposed by Zandt et al. (2004) of a negative buoyant root and an adjacent weakened zone.

2.1. Material model, density and viscosity

The modeled domain (Fig. 2a) includes eight different materials, each having a different reference density and/or rheology: (1) upper crust, (2) lower crust, (3) lithospheric mantle, (4) ultramafic batholithic root, (5) granitic batholith, (6) hydrated lithospheric mantle, (7) asthenosphere and (8) a low viscosity, low density top layer to mimic the free surface (Gerya and Yuen, 2003; Schmeling et al., 2008). We will refer to this last layer as the 'sticky air' layer adopting the terminology by Schmeling et al. (2008). The thickness and viscosity of the "sticky air" layer have been tested to insure that it allows the crustal surface to act as a free surface (see Section 1.2 on marker-topography). The initial distribution of temperature for the crust and lithospheric mantle is given by the steady-state solution of the heat conduction equation. For the asthenosphere we assume an adiabatic initial geotherm computed assuming a temperature of 1300 °C at the base of the lithosphere, and corresponding to a potential temperature of 1270 °C (Fig. 2b).

Density and viscosity are assumed to be temperature dependent in the lithospheric mantle and asthenosphere (Fig. 2b) and the boundary between these layers is assumed to be a thermal boundary with no compositional difference. The crustal layers are assigned a fixed density without temperature dependence, whereas for the mantle and lithosphere we use a simplified equation of state based on thermal expansion: $\rho=\rho_0(1-\alpha(T-T_{surf}))$, where, ρ_0 is the density at $T_{surf}=0$ °C for each material (Table 2). Note that a density of $\rho_0=3500\ kg/m^3$ is used for the ultramafic batholith to account for the high density of this eclogitic material.

While previous models have used sophisticated rheological models (e.g., Le Pourhiet et al. (2006)), we have chosen to use Newtonian viscosity to model the effective viscosities: therefore weak regions have a lower viscosity because of both composition and the presumed higher

Author's personal copy

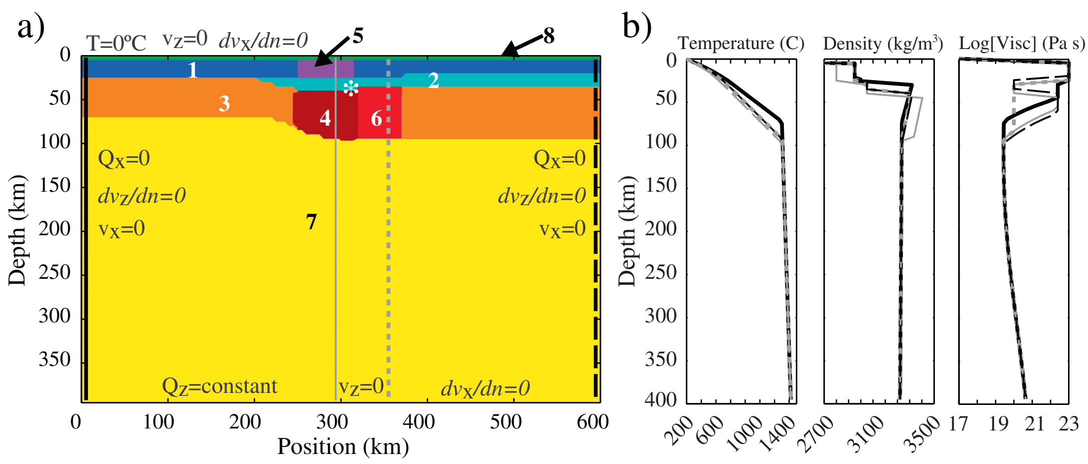

Fig. 2. Model geometry and materials. (a) Initial state and boundary conditions. The model includes eight different materials: (1) upper crust, (2) lower crust, (3) lithospheric mantle, (4) ultramafic batholithic root, (5) granitic batholith, (6) hydrated lithospheric mantle, (7) asthenosphere and (8) a low viscosity, low density 'sticky air' layer. Migration point used to track horizontal displacement of the lithosphere is marked by a white star at x = 315 km and depth = 45 km (top-east corner of ultramafic root). Vertical lines mark the location of depth profiles shown in the bottom panel (same color code and line style). (b) Initial profile for temperature, density and viscosity for the reference model at the leftmost side of the model (thick black), across the ultramafic batholith (gray), across the hydrated lithospheric mantle (thick dashed gray) and the rightmost side of the model (long-dash black).

strain-rates within some of these layers. The viscosity model uses constant (not temperature-dependent) values of the viscosity for each layer of the crust and the granitic batholith (see Table 2). For the lithosphere and asthenosphere we use a Newtonian temperature-dependent (exponential) viscosity law, augmented with a pressure dependence that crudely simulates an increase in deeper-mantle viscosity beneath 250 km (Rüpke et al., 2004):

$$\mu(T, z) = \mu_{ref}\mu(z)\exp\left[b\left(\frac{T_0}{T} - 1\right)\right] \tag{4}$$

$$\mu(z) = 1 + 124.5\{1 + \tanh[0.01(z - 450)]\} \tag{5}$$

where μ_{ref} is a reference viscosity for each material; b is a parameter characterizing the temperature dependence of viscosity; and T_0 is the reference temperature at the base of the lithospheric mantle. The values for these parameters are given in Table 1.

For the crust the constant viscosity value takes into account the assumed composition and its rheology for the pressure and temperature range of that layer. For example, in the eastern portion of the model domain, the lower crust is three orders of magnitude weaker than the upper crust, with a viscosity of 10^{20} Pa-s, as expected for a quartz-feldspar dominated composition (Burgmann and Dresen, 2008). Similarly, the maximum viscosity of the lithosphere and mantle is limited to 2.5×10^{22} Pa-s because this is consistent with olivine rheology and the strain-rates ($>10^{-14}$ s^{-1}) associated with deformation in the unstable or foundering lithosphere. Similarly the viscosity of the hydrated mantle–lithosphere is limited to 10^{20} Pa-s, consistent with a water content 100 times higher than normal 'dry' mantle–lithosphere. In addition, note that the main motivation for using this simplified rheologic structure is to allow us to easily test the effect of increasing or decreasing the viscosity of any one of the components of the model in order to determine its role in the dynamics.

Table 2
Values for the variables used for each material.

		Density ($kg\ m^{-3}$)	Viscosity (Pa s)
1	Upper crust	2850	10^{23}
2	Lower crust	2950	10^{20}
3	Lithospheric mantle	$3400(1 - \alpha(T - T_{surf}))$	$\mu_{ref} = 2.5 \times 10^{19}$ $\mu_{max} = 2.5 \times 10^{22}$
4	Ultramafic batholithic root	$3500(1 - \alpha(T - T_{surf}))$	$\mu_{ref} = 2.5 \times 10^{19}$ $\mu_{max} = 2.5 \times 10^{22}$
5	Granitic batholith	2700	10^{23}
6	Hydrated lithospheric mantle	$3400(1 - \alpha(T - T_{surf}))$	$\mu_{ref} = 2.5 \times 10^{19}$ $\mu_{max} = 10^{20}$
7	Asthenosphere	$3400(1 - \alpha(T - T_{surf}))$	$\mu_{ref} = 2.5 \times 10^{19}$ $\mu_{max} = 2.5 \times 10^{22}$
8	'Sticky air'	1	10^{17}

2.2. Methods used for analysis of model results

In order to present the evolution of the model in the clearest possible way, we show plots of the time-evolution of total kinetic energy of the system (KE–t plot). The total kinetic energy is computed considering the kinetic energy of all nodes. These plots are useful in characterizing the different phases of the lithosphere unrooting process (e.g., Marotta et al., 1998, 1999). We show that this KE–t plot can also characterize the evolution of the asymmetric removal process.

To model the evolution of dynamic topography we have included a highly buoyant upper layer of very low viscosity, following previous studies (e.g., Gerya and Yuen, 2003; Schmeling et al., 2008). This 'sticky air' layer has an initial thickness of 10 km and the interface between this layer and the top of the crust is assumed to behave as a free surface. The thickness and viscosity of the 'sticky air' layer are chosen to fulfill the criteria introduced by Crameri et al. (2012) to mimic a real free surface. We track motion of markers at this 'free surface' to compute changes in topography. We will refer to this computed topography as 'marker topography'. Although the term 'dynamic topography' is commonly used for topography computed in this way (e.g., Crameri et al., 2012) we prefer using the terms 'marker topography' as 'dynamic topography' is also sometimes defined to include only the non-isostatic response to flow-induced stresses, whereas the marker topography also has an isostatic component.

3. Results

As stated above we aim to test the rheological and density structure that controls the mode of asymmetric lithospheric foundering inferred for the southern Sierra Nevada, and specifically to test the hypothesis that weakening of the mantle lithosphere destabilized the batholithic root creating an east-dipping slab-shaped structure. We first present the reference model to illustrate the dynamics of foundering compatible with observations. We then discuss how the

Author's personal copy

time-dependent deformation in the reference model depends on the model structures and layer parameters. Finally, in the Discussion section, we discuss the model results in terms of implications for the southern Sierra Nevada.

3.1. Reference model evolution

The evolution of the reference model occurs in three stages (Figs. 3, 4) as illustrated in the KE–t plot (Fig. 5). In the first stage, from 0 to 5 My of evolution, the total kinetic energy increases exponentially. The upwelling of buoyant asthenosphere pushes the hydrated lithospheric material and the ultramafic root laterally westward. The ultramafic root, which starts tilting eastward and foundering, drags down some crustal material (Figs. 3a, b, 4a, b). Velocity of the westward propagation can be measured from the horizontal variation of the position of a point, that we call the 'migration point', which is initially located at the Moho at the right side (east) of the ultramafic batholith (at 315 km, 45 km depth; see location in Fig. 2a, and change in position in Figs. 3 and 4). The migration velocity, measured as the horizontal displacement of the migration point between timesteps, is initially 0.5 cm/y (0–3 My) and then increases up to 0.67 cm/y (3–6 My). The end of this stage coincides with a plateau in the maximum of total kinetic energy, at about 4–5 My (Fig. 5).

The crust and lithosphere delamination process predicts the occurrence of a double-branched Moho with a 'crocodile mouth' geometry characteristic of lithospheric delamination (Fig. 4b). It forms at the crustal thickening region, by the combination of two mechanisms: dragging of the crust by the sinking of the ultramafic batholith, and the westward inflow of asthenosphere (Fig. 4b). The doubled Moho appears after 4 My of evolution and it is very clear at 6 My (Figs. 3b and 4b). This 'bifurcated Moho' has been observed with receiver functions for the Colorado Plateau, where a progression of events very similar to the simulations presented here has also been proposed (Levander et al., 2011).

The second stage of model evolution, from 5 My to 11 My, is characterized by a decrease in the total kinetic energy (Fig. 5) as the ultramafic batholith stops rotating. The in-flowing asthenosphere continues to push the lithospheric material westward, but it cools down and increases its viscosity as it approaches the upper part of the mantle lithosphere (insets in Fig. 3b, c). The dense ultramafic batholith root sinks, dragging down lithospheric mantle and crustal material, and creates an east-dipping slab-shaped structure reaching depths of about 200 km at 9–10 My (Figs. 3c and 4c). During this stage, the 'migration velocity' is 0.67 cm/y at 6–9 My and then decreases to 0.3 cm/y at 9–12 My.

In the third stage, 10 My to 12 My, the lateral westward migration decreases and finally stops. The westernmost end of the lower crustal layer is reached at around 11 My, coinciding with a minimum of the total kinetic energy (Fig. 3c). In this stage the dense batholithic root sinks in situ and the slab-shaped lithospheric material is thermally and viscously eroded. This decrease in lateral migration is responsible for changing the crust–mantle boundary from the double-branched Moho into a V-shape crustal geometry (Figs. 3d, 4d). Finally, at about 12 My, vertical sinking of the root and delaminated lithosphere causes the system to accelerate again (Fig. 5).

In the reference model presented here, there is lithospheric mantle and crustal thinning in a 100 km wide region to the right of the migrating foundering root, where the asthenospheric material has replaced the hydrated lithospheric mantle. This crustal thickening/thinning pattern was also found in previous models (e.g., Göğüş and Pysklywec, 2008a,b; Schott and Schmeling, 1998; Valera et al., 2008) and it seems to be a characteristic feature of this kind of laterally migrating process.

Another important aspect of the asymmetric evolution illustrated in this reference model is the prediction of a zone of pronounced shear strain rate, between the crust and the foundering root, due to the strong flow of asthenospheric material (black box in Fig. 6). This region also has horizontally-oriented flow at the base of the crust (Fig. 4) with vertical gradients in magnitude. Therefore, this negative shear strain rate, created by a bottom-to-west flow (Fig. 4d) could lead to the development of

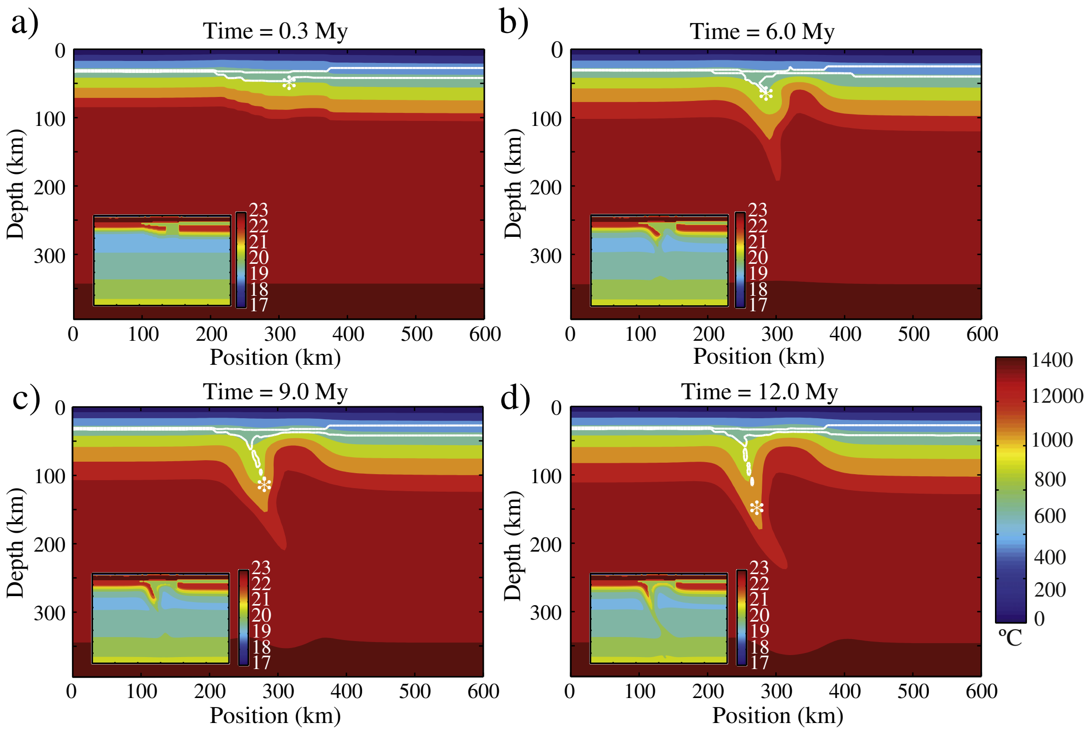

Fig. 3. Reference model evolution. Temperature (°C) and logarithm of viscosity (inset, Pa-s) at: a) 0.3 My, b) 6 My, c) 9 My and d) 12 My. White lines show the base of the upper and lower crust. Migration point used to track horizontal displacement of the lithosphere is marked by a white star.

Author's personal copy

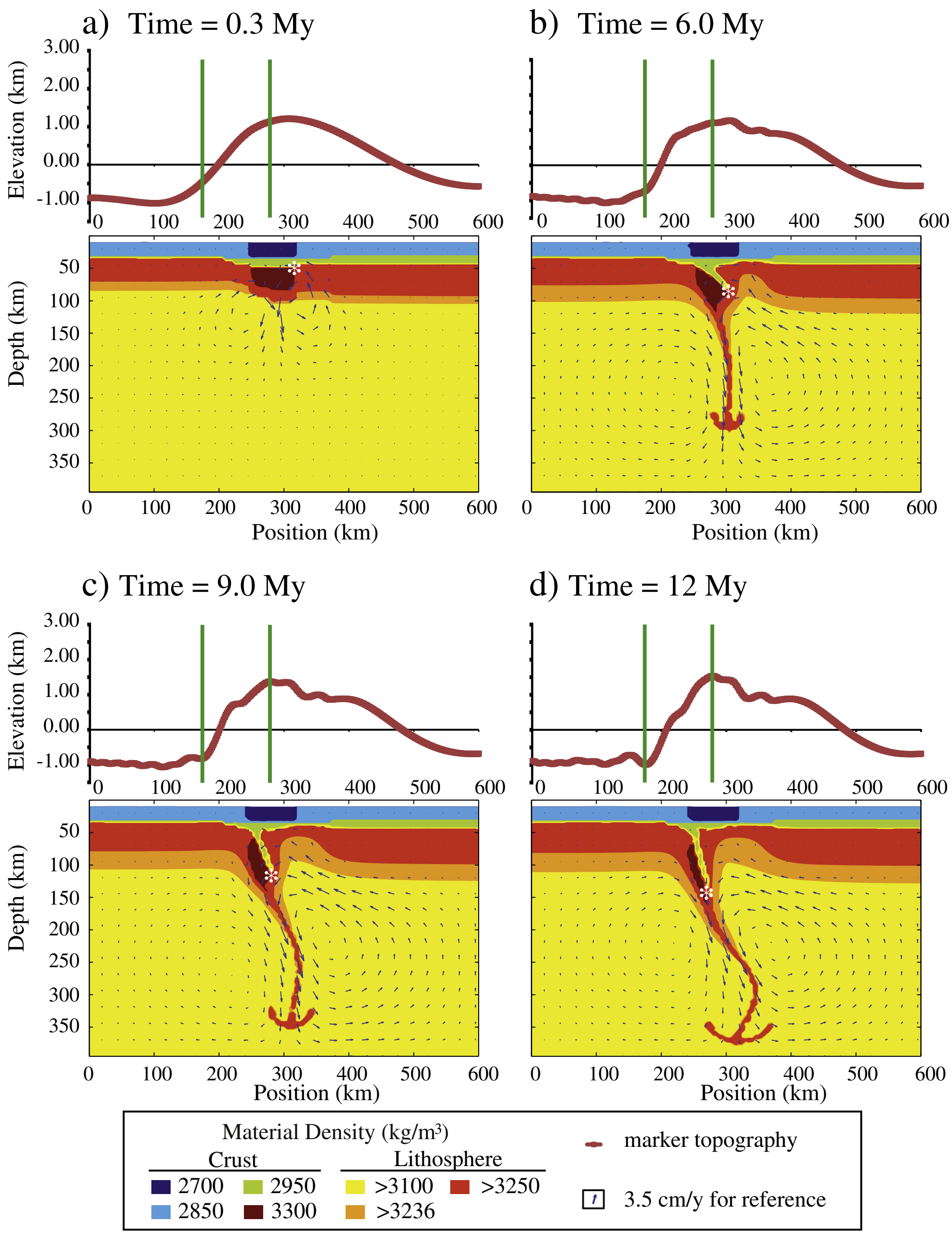

Fig. 4. Reference model evolution. Distribution for density (kg/m^3), marker topography at: a) 0.3 My, b) 6 My, c) 9 My and d) 12 My. Colors for materials are the same as in Fig. 2: crustal densities are fixed, while lithosphere densities are temperature dependent. Green vertical lines on the topography figures mark the location of points of maximum subsidence (x = 177 km) and uplift (x = 280 km) plotted versus time in Fig. 7. Migration point used to track horizontal displacement of the lithosphere is marked by a white star.

anisotropic fabric in the mantle just below the newly formed crust–mantle boundary. In order to confirm this result, it is necessary to calculate the cumulative strain through this region and the orientation of the stretching axis (e.g., see Kaminski and Ribe (2002)).

3.2. Reference model topographic response

We have computed the marker topography at different time-steps of the evolution. The marker topography is computed from the motion of the markers at the interface between the 'sticky air' layer and the upper crust. We must stress that model predicted topography depends on the chosen parameter set (densities and viscosities of each material). Moreover, complexities such as plasticity and strain localization are not taken into account in the simple viscous approach adopted here. For these reasons, topographic predictions are not to be compared directly with real elevation data, but with regional trends of uplift or subsidence in space and time.

Marker topography has an initial transient rapid response to attain isostatic equilibrium and is consistently high from a position of about 200 to 450 km starting in the initial stage (Fig. 4a), indicating the prevailing effect of the buoyant granitic batholith. The pull exerted by the foundering of the ultramafic batholithic root produces a maximum subsidence in marker topography at position 177 km (left vertical line in Fig. 4), which becomes more evident after 12 My (Fig. 4d, present day). This subsidence is of dynamic origin as it is not directly above the foundering root, but shifted westward. It therefore corresponds to

Author's personal copy

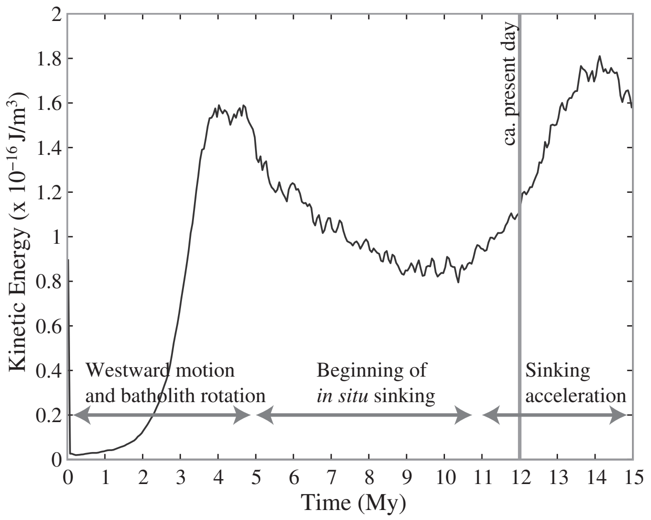

Fig. 5. Reference model KE–t plot. Time evolution of the total kinetic energy of the system (KE–t plot) illustrating the three main stages of evolution for the asymmetric removal process: 1) westward motion of batholithic root leads to peak in total kinetic energy, followed by 2) beginning of in situ sinking and a decrease in total kinetic energy, and finally 3) sinking acceleration marked by a second peak in total kinetic energy.

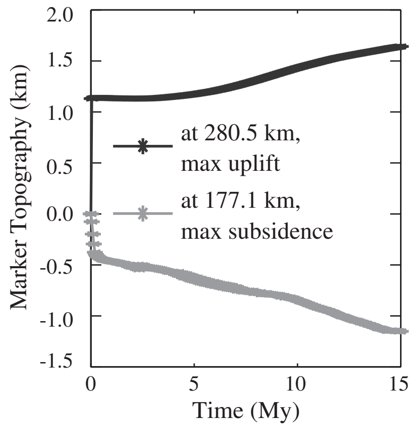

Fig. 7. Reference model time evolution of topography. Marker topography as a function of time for the point of maximum uplift (x = 280.5 km) with two stages of uplift and maximum subsidence (x = 177 km) with monotonous subsidence following an initial transient.

an oblique propagation of the pull exerted by the sinking ultramafic root and lithosphere. The topographic evolution of this point has a rather constant subsidence rate of 52 m/My, after an initial transient (Fig. 7).

As the ultramafic batholith is progressively detached from the crust and is progressively replaced by hotter and lighter material, the uplifted region over the granitic batholith further increases in the marker topography (Figs. 4d, 7). The maximum uplift in marker topography (at 280.5 km) does not occur over the area of asthenospheric upwelling, but above a zone of thickened lower crust, some 30 km east of the vertex of the V-shaped Moho. This suggests that uplift is mainly due to the removal of the dense ultramafic root from below the buoyant granitic batholith, rather than to asthenospheric upwelling. Also, marker topography consistently decreases to the east of the granitic batholith ($x > 330$ km). The region of predicted topographic uplifted is localized above the batholith, however this would be broader and lower amplitude if the visco-elastic response of the lithosphere was taken into account.

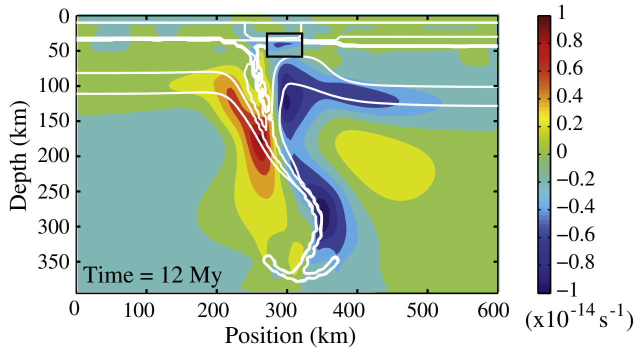

Fig. 6. Reference model shear strain-rate at 12 My. Colors indicate the shear strain rate distribution ($\dot{e}_{xz}$, s^{-1}), with positive values indicating rightward (increasing position direction) strain. White lines show the outlines of the same density fields shown in Fig. 4d for reference. Note pronounced shear strain zone between the crust and the foundering root (black box: density contours have been removed within the box for clarity) that reflects the strong westward flow due to asthenospheric upwelling and localized horizontal shear at the base of the crust.

The point of maximum uplift shows two different stages of uplift (Fig. 7). The first stage, 0 to 5 My, corresponds to an almost stable high topography. The second stage begins after about 5 My of evolution and it is characterized by an uplift rate of 47 m/My and is the result of the mechanical decoupling of the granitic batholith from its ultramafic root (Fig. 4b) and significant asthenospheric inflow.

3.3. Parametric study

Our choice of the reference model parameters is based on a parametric study that we summarize in this section to illustrate where the reference model sits in the parameter space, and the role of different parameters in creating the dynamics. We have explored two different types of parametric studies modifying, a) the presence or absence of some of the controlling bodies (Models a–d: granitic and ultramafic batholiths and hydrated lithospheric mantle) and b) the value of viscosity or density for lower crust (Models B1–B5: viscosity of the lower crust; Models C1–C4: density of the lower crust) and the maximum viscosity of the lithospheric mantle (Models D1–D7). A total of 23 models were tested (Fig. 8).

To quantify the difference in dynamics for different model parameters we compare the horizontal displacement of the migration point after 12 My of evolution versus the depth reached by the 1200 °C isotherm at the same time (Fig. 8: the reference model is denoted by a blue star). The time of 12 My is chosen as it corresponds to the present-day in the context of the evolution of the southern Sierra Nevada. In this figure, the delamination sensu stricto mechanism (in the sense of Bird (1978)) should appear near the right-bottom corner, with both high horizontal displacements and deep sinking of the slab-like structure. In contrast, the 'convective removal' (Rayleigh–Taylor instability) mechanism should appear near the left-bottom corner, with negligible horizontal displacement, but still high depths of the sinking lithosphere. Also, note that the maximum amount of horizontal displacement is limited by the initial viscosity structure, which takes into account the different crustal origins for the fore-arc lithosphere (no weak lower crust) and the adjoining continent (thicker crust with a weak lower crust).

3.3.1. Effect of different bodies

The absence of the granitic batholith (Model b) does not modify the evolution of asymmetric foundering (Fig. 8). However, it does result in a decrease in topography with respect to the reference model of about 500 m and 300 m for the locations of maximum and minimum elevation, respectively. In contrast, in the absence of the weak lower crust

Author's personal copy

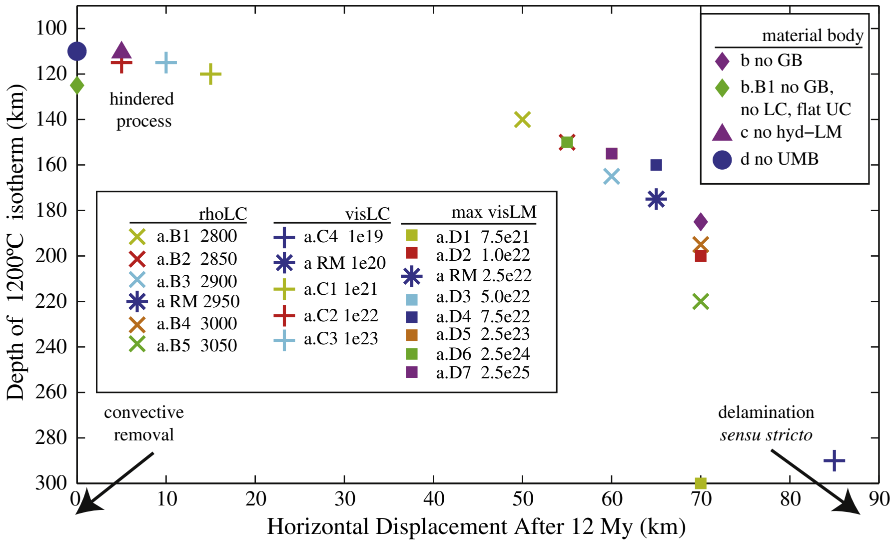

Fig. 8. Model dynamics summary for parametric study. Depth (km) reached by the 1200 °C isotherm versus the horizontal displacement of the migration point (km) after 12 My of evolution. Twenty-three models are presented to show the effects of the presence/absence of different bodies (Models b, b.B1, c, and d) and of varying the value of the lower crustal (LC) density (Models a.B1–B5, labeled rho) or viscosity (Models a. C1–C4, labeled vis) and the lithospheric mantle (LM) viscosity (Models a.D1–D7: a.D5 plots under a.D7). The blue star denotes the reference model (RM). Units are omitted for clarity but all are in the International System. UC is upper crust; hyd-LM is hydrated lithosphere; GB is Granitic Batholith; UMB is ultramafic batholith. In this figure, the delamination sensu stricto mechanism (in the sense of Bird (1978)) appears at the far right, bottom corner, with high horizontal displacements and high depths for the slab-like structure. The convective removal mechanism appears at the far left bottom corner, with high depths of the sinking lithosphere but negligible horizontal displacement. Models that appear at left top corner represent a hindered process, as neither sinking nor lateral migration occurs.

(Model b.B1) or the weak hydrated lithospheric mantle (Model c) or the ultramafic batholith (Model d), the foundering does not occur by any mechanism (Fig. 8). These models appear at the top left corner of Fig. 8: there is neither sinking nor migration, as they represent a hindered process.

These models demonstrate that geodynamic evolution represented by the reference model is controlled by three features: 1) the presence of the ultramafic batholith, the dense body that drags down the lithospheric material, 2) the presence of a low viscosity lower crust, which enables detachment of the lithosphere, and 3) the presence of hydrated lithospheric mantle adjacent to the ultramafic batholith, which through its inherent weakness allows asthenosphere to flow upwards.

3.3.2. Effect of viscosity structure and lower crust density

The density of the lower crust has a mediating affect on the deformation illustrated by the reference model. Although there is no change in the qualitative behavior, a denser lower crust (Models a.B4 and a.B5) speeds up the delamination process and allows for larger horizontal displacements and higher depths of the slab-like structure (Fig. 8). The contrary occurs for lower crustal density (Models a.B1, a. B2 and a.B3), which all have smaller horizontal displacements and lower depths of the slab-like structure at 12 My in the models. These lower crustal density models do eventually evolve to higher displacements and depths, but the model evolution is slower.

While lower crustal density has only a moderate effect on the mantle flow, the deformation is very sensitive to the viscosity value for this layer. Decreasing the lower crustal viscosity by one order of magnitude with respect to the reference model (Model a.C4) leads to a strong acceleration of the sinking, reaching higher depths and the largest horizontal displacements for 12 My of model evolution (Fig. 8). This acceleration is illustrated in the KE–t plot (Fig. 9) where a second maximum is reached about 3 My earlier than in the reference model. Similarly, an increase in lower crustal viscosity by only one order of magnitude with respect to the reference model (Model a.C1) means that the lower crust is so viscous that almost no displacement is allowed and only a thin layer of low viscosity (warm) lithospheric mantle drips (Fig. 8). This kind of hindered process is characterized by the absence of the second maximum in the KE–t plot (Fig. 9).

Finally, the model deformation is also sensitive to the maximum viscosity allowed for the lithospheric mantle. A decrease of only half an order of magnitude with respect to the reference model (Model a.D1) leads to a strong acceleration of sinking (Fig. 8) and an earlier occurrence of the second maximum in the KE–t plot (Fig. 9). In contrast the same increase in maximum viscosity (Model a.D4) does not change the deformation pattern significantly (Fig. 8) because this increase only affects a relatively thin layer of the uppermost lithospheric mantle. On the basis of this parametric analysis, a value of the maximum effective lithospheric viscosity of

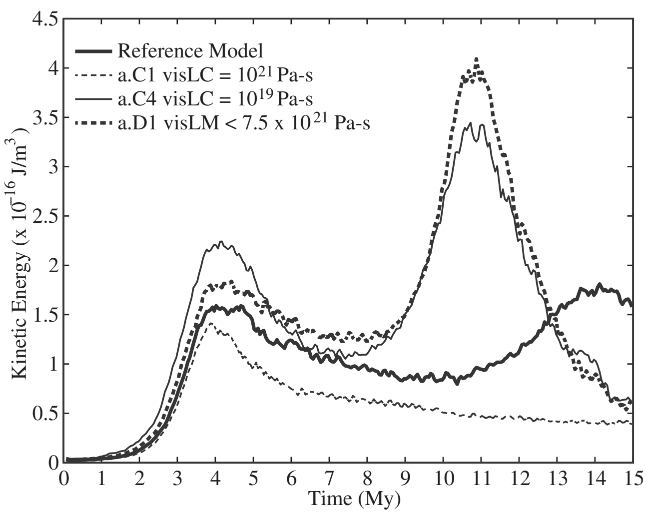

Fig. 9. KE–t plot for end-member models. Time-evolution of total kinetic energy of the system: the reference model (RM, thick black), Model a.C1 (stronger lower crust: visLC $= 10^{21}$ Pa-s, dashed black), Model a.C4 (weaker lower crust: visLC $= 10^{19}$ Pa-s, thin black), and Model a.D1 (weaker lithospheric-mantle, viscLM $< 7.5 \times 10^{21}$ Pa-s, thick-dashed black).

Author's personal copy

2.5×10^{22} Pa s was adopted for the reference model because this value leads to a final mantle structure (slab-like body dip and depth) consistent with tomographic images for the Isabella Anomaly in the southern Sierra Nevada.

4. Discussion

The modeling presented is not intended to provide a unique and definitive set of parameters to be used to predict the complete evolution of the Sierra Nevada. In particular, while we purposely use simplified Newtonian rheology in order to allow for easier comparison of different model structure, a non-Newtonian rheology with elasto-plastic rheology is certainly more appropriate and could modify some of the results presented here. In addition, the observations indicate that the foundering process is likely three-dimensional and this could affect the timing and geometry of structures that develop during the foundering process. Therefore, the models presented are intended to numerically evaluate the laterally migrating foundering hypothesis, initially inspired by the conceptual model proposed by Zandt et al. (2004), and to compare model predictions with observations, in an effort to understand the role played by the granitic and ultramafic batholiths and the effect of lithospheric structure on the topographic response.

4.1. General model dynamics

The controlling features in the models presented here, a weak lower crust and a weak (hydrated) lithospheric-mantle region adjacent to the dense root, are also key factors in the models by Le Pourhiet et al. (2006). However, the deformation pattern and timing of sinking predicted by both approaches are quite different. First, Le Pourhiet et al. (2006) predict a phase (from 11 to 6 Ma) of asthenospheric spreading along the base of the crust, without ultramafic root sinking, which occurs later at about 2 Ma. In the reference model presented here, sinking of the ultramafic root develops earlier, at 12 Ma to 8 Ma before present, and promotes further asthenospheric material ascent. Therefore, in contrast to the models by Le Pourhiet et al. (2006), both root sinking and asthenospheric lateral upwelling occur simultaneously as a result of development of a counter-clockwise advection cell (Fig. 4a).

Therefore, the model by Le Pourhiet et al. (2006) is similar to the delamination process as described by Bird (1978, 1979; also called delamination sensu stricto, e.g., Calvert et al., 2000) whereas the dynamics of the asymmetric foundering modeled here is governed by the interplay between the westward push exerted by rising asthenospheric material and the downward force of the negative buoyancy of the dense batholithic root.

The differences in the model evolution of these two studies are captured by the rate of delamination as quantified by the horizontal migration velocities. Bird and Baumgardner (1981) modeled the propagation of delamination using a moving reference frame, which follows the delamination front and assuming steady state. They found horizontal displacement velocities ranging from 0.8 to 5.3 cm/y for a 200 km long slab and different configurations. Morency and Doin (2004) reported velocities varying between 0.2 and 10 cm/y. The migration velocities of 0.5–0.67 cm/y for the reference model are close to the lower bound of the range of values found by previous studies, and reflect a slowly migrating foundering process controlled by the viscosity of the lower crust, which limits the rate of westward asthenospheric flow into the opening low viscosity crustal channel. These velocities are sensitive to the viscosity and density of the lower crust and to the mass of the sinking lid (see Fig. 8).

Accordingly, this type of slowly migrating foundering process lies in between two end-members: a process with strong lateral intrusion of asthenospheric material along the base of the crust (delamination sensu stricto); and a process of sinking in situ of a dense root, without any lateral intrusion of asthenosphere (i.e. convective root removal, e.g., Harig et al., 2008; Houseman et al., 1981).

4.2. Application to the southern Sierra Nevada

In comparing the reference model evolution with the suite of seismic observations, we find good agreement for a wide range of independent constraints on the subsurface structure (Fig. 1). First, the predicted foundering root shape and depth are consistent with the high seismic velocity anomaly imaged in the region (Boyd et al., 2004; Schmandt and Humphreys, 2010). Second, both the V-shape and the 50 km depth predicted for the Moho above the downwelling are consistent with the inferences from receiver function seismology below the western foothills (Frassetto et al., 2011; Gilbert et al., 2007; Zandt et al., 2004). Third, the 100-km wide region of lithospheric mantle and crustal thinning to the right (east) of the migrating foundering root is consistent with receiver function studies showing a broad region of shallow, rejuvenated Moho east and northeast of the Isabella anomaly (Frassetto et al., 2011). And, finally the development of strong negative shear strain rate below the crust is consistent with the location and orientation of observed anisotropic fabrics, inferred from receiver function analysis (Zandt et al., 2004).

Similarly, the evolution of surface topography agrees well with present-day observations as well as constraints on the timing and stages of uplift in the southern Sierra Nevada. First, the location of model-predicted subsidence, above the foundering root occurs about 80 km west of the area of the V-shape Moho, and roughly agrees with the location of Tulare Basin (Fig. 1). This spatial correlation may provide further support to the idea that the Tulare Basin subsidence is caused by viscous drag of the sinking drip (Zandt et al., 2004). Second, the reference model predicts a monotonous topographic increase of about 400 m of the higher areas beginning after 5 My of evolution (corresponding to ~7 Ma if we assume that present day corresponds to about 12 My of evolution), and a monotonous decrease of low areas of about 615 m since 12 Ma (Fig. 7). This timing of uplift is in agreement with the timing of the first phase of uplift characterized by Clark et al. (2005) to have occurred between 32 Ma and 3.5 Ma, and thought to be related to dripping or delamination (Bennett et al., 2009), whereas the second later phase of uplift since 3.5 Ma is due to a possible flexural response (Bennett et al., 2009) and cannot be accounted for here as we have not included elasticity in these models.

An additional difference between the models presented here and the model by Le Pourhiet et al. (2006) is the role of imposed crustal extension. In our models there is no imposed crustal extension, and therefore, while crustal extension was occurring in the Sierra Nevada at this time, we find that this is not a necessary condition to match the observations.

Finally, an important limitation of the application of these model results to Sierra Nevada is the clear 3D nature of the observations and the use of 2D numerical simulations. As the 2D results demonstrate that the initial structure of the lithosphere and crust, both in terms of density and viscosity, controls how the deformation process occurs, the 3D pattern of shallow crust imaged beneath the Sierra Nevada may reflect the initial location of a weak hydrated crust adjacent to the batholithic root and subsequent removal of this material. This also suggests that the fast seismic velocity anomaly formed from a more complex 3D delamination of the lithosphere, migrating both west and south, and asthenospheric flow infiltrating the expanding gap from multiple directions.

5. Conclusions

In this study we have quantitatively evaluated, by means of thermo-mechanical modeling, the timescale and final geometry of asymmetric foundering of a high-density root. The predicted dynamics is controlled by: a) the upwelling of buoyant asthenosphere

Author's personal copy

facilitated by the presence of a weakened lithospheric mantle region adjacent to a dense batholithic root, b) the westward inflow enabled by a low viscosity lower crust, and c) negative buoyancy of the dense root. The dynamics of lithospheric foundering that occur can be characterized as a migration process slowed by the rate at which asthenospheric material can flow into a weak lower crust channel: this behavior lies between end-member models of pure delamination and Rayleigh–Taylor instability. The resulting asymmetric foundering leads to an east-dipping slab-shaped lithospheric mantle downwelling, spatial variation in crustal structure and surface topography history that is in agreement with a wide range of observations for the southern Sierra Nevada.

Acknowledgments

This work was funded by the Spanish Plan Nacional del MCINN project CGL2009-13103, CGL2009-09662 and CGL2012-37222. This is a contribution of the Consolider-Ingenio 2010 team CSD2006-00041 (TOPO-IBERIA). M. I. Billen acknowledges support from NSF grants 6877321 and 0748818. Simulations were partly carried out in the Fiswulf cluster of the Faculty of Physics. Part of this manuscript was written during a postdoctoral stage of J. L. Valera in the Goethe University, in Frankfurt am Main. We acknowledge helpful comments from Harro Schmeling.

References

Anderson, J.D., 1995. Computational Fluid Dynamics. McGraw Hill, Inc.

Andrews, E., Billen, M.I., 2009. Rheologic controls on slab detachment. Tectonophysics (Special Volume on Slab Detachment) 464, 60–69. http://dx.doi.org/10.1016/j.tecto.2007.09.004.

Atwater, T., Stock, J., 1998. Pacific-North America, plate tectonics of the Neogene southwestern United, States: an update. International Geological Review 40, 375–402.

Bajolet, F., Galeano Prieto, J., Funiciello, F., Moroni, M., Negredo, A.M., Faccenna, C., 2012. Continental delamination: insights from laboratory models. Geochemistry, Geophysics, Geosystems (G^3). http://dx.doi.org/10.1029/2011GC003896.

Beck, S.L., Zandt, G., 2002. The nature of orogenic crust in the central Andes. Journal of Geophysical Research 107 (B10), 2230. http://dx.doi.org/10.1029/2000JB000124.

Bennett, R.A., Fay, N.P., Hreinsdóttir, S., Chase, C., Zandt, G., 2009. Increasing long-wavelength relief across the southeastern flank of the Sierra Nevada, California. Earth and Planetary Science Letters 287, 255–264.

Bird, P., 1978. Initiation of intracontinental subduction in the Himalaya. Journal of Geophysical Research 83, 4975–4987.

Bird, P., 1979. Continental delamination and the Colorado Plateau. Journal of Geophysical Research 84, 7561–7571.

Bird, P., Baumgardner, J., 1981. Steady propagation of delamination events. Journal of Geophysical Research 86, 4891–4903.

Bohannon, R.G., Parsons, T., 1995. Tectonic implications of post-30 Ma Pacific and North American relative plate motions. Geological Society of America Bulletin 107, 937–959. http://dx.doi.org/10.1130/0016-7606(1995)107 < 0937:TIOPMP > 2.3.CO;2.

Boyd, O.S., Jones, C.H., Sheehan, A.F., 2004. Foundering lithosphere imaged beneath the southern Sierra Nevada, California, US. Science 305, 660–662.

Burgmann, R., Dresen, G., 2008. Rheology of the lower crust and upper mantle: evidence from rock mechanics. Geodesy and field observations. 36, 531–567.

Calvert, A., Sandvol, E., Seber, D., Barazangi, M., Roecker, S., Mourabit, T., Vidal, F., Alguacil, G., Jabour, N., 2000. Geodynamic evolution of the lithosphere and upper mantle beneath the Alboran Region of the Western Mediterranean: constraints from travel time tomography. Journal of Geophysical Research 105, 10871–10898.

Channel, J.E.T., Mareschal, J.C., 1989. Delamination and asymmetric lithospheric thickening in the development of the Thyrrhenian Rift, in Alpine Tectonics. In: Coward, M.P., Dietrich, D., Park, R.G. (Eds.), Geol. Soc. Lond. Spec. Publ., 45, pp. 285–300.

Clark, M.K., Mahéo, G., Saleeby, J., Farley, K.A., 2005. The nonequilibrium landscape of the southern Sierra Nevada, California. Geological Society of America Today 15, 4–10.

Crameri, F., Schmeling, H., Golabek, G.J., Duretz, T., Orendt, R., Buiter, S.J.H., May, D.A., Kaus, B.J.P., Gerya, T.V., Tackley, P.J., 2012. A comparison of numerical surface topography calculations in geodynamic modeling: an evaluation of the 'sticky air' method. Geophysical Journal International 189 (1), 38–54. http://dx.doi.org/10.1111/j.1365-246X.2012.05388.x.

Ducea, M.N., 2001. The California arc: thick granitic batholiths, eclogitic residues, lithospheric-scale thrusting, and magmatic flare-ups. Geological Society of America Today 11, 4–10. http://dx.doi.org/10.1130/1052-5173(2001)011 < 0004:TCATGB > 2.0.CO;2.

Ducea, M.N., Saleeby, J.B., 1996. Buoyancy sources for a large, unrooted mountain range, the Sierra Nevada, California: evidence from xenolith thermobarometry. Journal of Geophysical Research 101, 8229–8244.

Ducea, M.N., Saleeby, J.B., 1998a. A case for delamination of the deep batholithic crust beneath the Sierra Nevada, California. International Geological Review 40 (1), 78–93.

Ducea, M.N., Saleeby, J.B., 1998b. Crustal recycling beneath continental arcs: silica-rich glass inclusions in ultramafic xenoliths from the Sierra Nevada, California. Earth and Planetary Science Letters 156, 101–116.

Duggen, S., Hoernle, K., van den Bogaard, P., Rüpke, L., Phipps-Morgan, J., 2003. Deep roots of the Messinian salinity crisis. Nature 422, 602–606.

Elkins-Tanton, L., 2007. Continental magmatism, volatile recycling and a heterogeneous mantle caused by lithospheric gravitational instabilities. Journal of Geophysical Research 112, B03405. http://dx.doi.org/10.1029/2005JB004072.

England, P.C., Houseman, G.A., 1989. Extension during continental convergence, with application to the Tibetan Plateau. Journal of Geophysical Research 94, 17561–17579. http://dx.doi.org/10.1029/JB094iB12p17561.

Faccenda, M., Minelli, G., Gerya, T.V., 2009. Coupled and decoupled regimes of continental collision: numerical modeling. Earth and Planetary Science Letters 278, 337–349. http://dx.doi.org/10.1016/j.epsl.2008.12.021.

Farmer, G.L., Glazner, A.F., Manley, C., 2002. Did lithospheric delamination trigger late Cenozoic potassic volcanism in the Sierra Nevada, California? Geological Society of America Bulletin 114, 754–768.

Figueroa, A.M., Knott, J.R., 2010. Tectonic geomorphology of the southern Sierra Nevada Mountains (California): evidence for uplift and basin formation. Geomorphology 123, 34–45. http://dx.doi.org/10.1016/j.geomorph.2010.06.009.

Fillerup, M.A., Knapp, J.H., Knapp, C.C., Raileanu, V., 2010. Mantle earthquakes in the absence of subduction? Continental delamination in the Romanian Carpathians. Lithosphere 2 (5), 333–340. http://dx.doi.org/10.1130/L102.1.

Fliedner, M., Klemperer, S.L., Christensen, N.I., 2000. Three-dimensional seismic model of the Sierra Nevada arc, California, and its implications for crustal and upper mantle composition. Journal of Geophysical Research 105, 10899–10921.

Forsyth, D.W., Rau, C.J., 2009. Isabella anomaly: lithospheric drip, delamination or fragment of the Farallon plate. Eos, Transactions of the American Geophysical Union 90 (52).

Frassetto, A.M., Zandt, G., Gilbert, H., Owens, T.J., Jones, C.H., 2011. Structure of the Sierra Nevada from receiver functions and implications for lithospheric foundering. Geosphere 7 (4), 898–921. http://dx.doi.org/10.1130/GES00570.1.

Furlong, K.P., Kamp, P.J.J., 2009. The lithospheric geodynamics of plate boundary transpression in New Zealand: initiating and emplacing subduction along the Hikurangi margin, and the tectonic evolution of the Alpine Fault system. Tectonophysics 474, 449–462. http://dx.doi.org/10.1016/j.tecto.2009.04.023.

Gemmer, L., Houseman, G.A., 2007. Convergence and extension driven by lithospheric gravitational instability: evolution of the Alpine–Carpathian–Pannonian system. Geophysical Journal International 168, 1276–1290.

Gerya, T., Yuen, D.A., 2003. Rayleigh–Taylor instabilities from hydration and melting propelled 'cold plumes' at subduction zones. Earth and Planetary Science Letters 212, 47–62.

Gilbert, H., Jones, C., Owens, T.J., Zandt, G., 2007. Imaging Sierra Nevada lithosphere sinking. Eos, Transactions of the American Geophysical Union 88 (21), 225–229.

Göğüş, O.H., Pysklywec, R.N., 2008a. Near-surface diagnostics of dripping or delaminating lithosphere. Journal of Geophysical Research 113, B11404. http://dx.doi.org/10.1029/2007JB005123.

Göğüş, O.H., Pysklywec, R.N., 2008b. Mantle lithosphere delamination driving plateau uplift and syn-convergent extension in eastern Anatolia. Geology 36 (9), 723–726. http://dx.doi.org/10.1130/G24982A.1.

Göğüş, O.H., Pysklywec, R.N., Corbi, F., Faccenna, C., 2011. The surface tectonics of mantle lithosphere delamination following ocean lithosphere subduction: insights from physical-scaled analogue experiments. Geochemistry, Geophysics, Geosystems (G^3) 12, Q05004. http://dx.doi.org/10.1029/2010GC003430.

Harig, C., Molnar, P., Houseman, G.A., 2008. Rayleigh–Taylor instability under a shear stress free top boundary condition and its relevance to removal of mantle lithosphere from beneath the Sierra Nevada. Tectonics 27, TC6019.

Henry, C.D., 2009. Uplift of the Sierra Nevada, California. Geology 37, 575–576. http://dx.doi.org/10.1130/focus062009.1.

Houseman, G., Molnar, P., 2001. Mechanisms of lithospheric rejuvenation associated with continental orogeny. In: Miller, J.A., Holdsworth, R.E., Buick, I.S., Hand, M. (Eds.), Continental Reactivation and Reworking, 184. Geological Society, London, Special Publications, London, pp. 13–38.

Houseman, G., Mackenzie, D., Molnar, P., 1981. Convective instability of a thickened boundary layer and its relevance for the thermal evolution of continental belts. Journal of Geophysical Research 86 (B7), 6115–6132. http://dx.doi.org/10.1029/JB086iB07p06115.

Ita, J., King, S.D., 1994. Sensitivity of convection with an endothermic phase change to the form of governing equations, initial conditions, boundary conditions and equation of state. Journal of Geophysical Research 99, 15919–15938.

Jiménez-Munt, I., Platt, J.P., 2006. Influence of mantle dynamics on the topographic evolution of the Tibetan Plateau: results from numerical modeling. Tectonics 25, TC6002. http://dx.doi.org/10.1029/2006TC001963.

Jones, C.H., Kanamori, H., Roecker, S.W., 1994. Missing roots and mantle "drips": regional Pn and teleseismic arrival times in the southern Sierra Nevada and vicinity, California. Journal of Geophysical Research 99 (B3), 4567–4601.

Kaminski, É., Ribe, N.M., 2002. Timescales for the evolution of seismic anisotropy in mantle flow. Geochemistry, Geophysics, Geosystems 3 (1051).

Kay, R.W., Kay, S.M., 1993. Delamination and delamination magmatism. Tectonophysics 219, 177189. http://dx.doi.org/10.1016/0040-1951(93)90295-U.

Knapp, J.H., Knapp, C.C., Raileanu, V., Matenco, L., Mocanu, V., Dinu, C., 2005. Crustal constraints on the origin of mantle seismicity in the Vrancea Zone, Romania: the case for active continental lithospheric delamination. Tectonophysics 410, 311–323.

Le Pourhiet, L., Gurnis, M., Saleeby, J., 2006. Mantle instability beneath the Sierra Nevada Mountains in California and Death Valley extension. Earth and Planetary Science Letters 251, 104–119.

Lee, C.-T., Yin, Q.-Z., Rudnick, R.L., Chesley, J.T., Jacobsen, S.B., 2000. Re–Os isotopic evidence for pre-Miocene delamination of lithospheric mantle beneath the Sierra Nevada, California. Science 289, 1912–1916.

Author's personal copy

Lee, C.-T., Rudnick, R.L., Brimhall Jr., G.H., 2001. Deep lithospheric dynamics beneath the Sierra Nevada during the Mesozoic and Cenozoic as inferred from xenolith petrology. Geochemistry, Geophysics, Geosystems (G^3) 2 (12). http://dx.doi.org/10.1029/2001GC000152.

Levander, A., Schmandt, B., Miller, M.S., Liu, K., Karlstrom, K.E., Crow, R.S., Lee, C.-T., Humphreys, E.D., 2011. Continuing Colorado plateau uplift by delamination-style convective lithospheric downwelling. Nature 472, 461–465. http://dx.doi.org/10.1038/nature10001.

Lorinczi, P., Houseman, G.A., 2009. Lithospheric gravitational instability beneath the Southeast Carpathians. Tectonophysics 474, 322–336. http://dx.doi.org/10.1016/j.tecto.2008.05.024.

Mahéo, G., Saleeby, J., Saleeby, Z., Farley, K.A., 2009. Tectonic control on southern Sierra Nevada topography, California. Tectonics 28, TC6006. http://dx.doi.org/10.1029/2008TC002340.

Marotta, A.M., Fernández, M., Sabadini, R., 1998. Mantle unrooting in collisional settings. Tectonophysics 296, 31–46.

Marotta, A.M., Fernàndez, M., Sabadini, R., 1999. The onset of extension during lithospheric shortening: a two-dimensional thermomechanical model for lithospheric unrooting. Geophysical Journal International 139, 98–114.

Molnar, P., Garzione, C.N., 2007. Bounds on the viscosity coefficient of continental lithosphere from removal of mantle lithosphere beneath the Altiplano and Eastern Cordillera. Tectonics 26, TC2013. http://dx.doi.org/10.1029/2006TC001964.

Molnar, P., Jones, C.H., 2004. A test of laboratory based rheological parameters of olivine from an analysis of late Cenozoic convective removal of mantle lithosphere beneath the Sierra Nevada, California, USA. Geophysical Journal International 156 (3), 555–564.

Morency, C., Doin, M.-P., 2004. Numerical simulations of the mantle lithosphere delamination. Journal of Geophysical Research 109, B03410. http://dx.doi.org/10.1029/2003JB002414.

Negredo, A.M., Valera, J.L., Carminati, E., 2004. TEMSPOL: a MATLAB thermal model for deep subduction zones including major phase transformations. Computers and Geosciences 30, 249–258.

Platt, J.P., Vissers, R.L.M., 1989. Extensional collapse of the thickened continental lithosphere: a working hypothesis for the Alboran Sea and Gibraltar Arc. Geology 17, 540–543.

Rüpke, L.H., Phipps-Morgan, J., Hort, M., Connolly, J.A.D., 2004. Serpentine and the subduction zone water cycle. Earth and Planetary Science Letters 223, 17–34.

Ruppert, S., Fliedner, M.M., Zandt, G., 1998. Thin crust and active upper mantle beneath southern Sierra Nevada. Tectonophysics 286, 237–252.

Saleeby, J., Ducea, M., Clemens-Knott, D., 2003. Production and loss of high-density batholithic root, southern Sierra Nevada, California. Tectonics 22 (6), 1064. http://dx.doi.org/10.1029/2002TC001374.

Schmandt, B., Humphreys, E., 2010. Seismic heterogeneity and small-scale convection in the southern California upper mantle. Geochemistry, Geophysics, Geosystems (G^3) 11 (5), Q05004. http://dx.doi.org/10.1029/2010GC003042.

Schmeling, H., 1989. Compressible convection with constant and variable viscosity: the effect on slab formation, geoid and topography. Journal of Geophysical Research 94 (B9), 12463–12481.

Schmeling, H., Babeyko, A., Enns, A., Faccenna, C., Funiciello, F., Gerya, T., Golabek, G., Grigull, S., Kaus, B., Morra, G., van Hunen, J., 2008. A benchmark comparison of spontaneous subduction models — towards a free surface. Physics of the Earth and Planetary Interiors 171, 198–223.

Schott, B., Schmeling, H., 1998. Delamination and detachment of a lithospheric root. Tectonophysics 296, 225–247.

Schubert, G., Turcotte, D.L., Olson, P., 2001. Mantle Convection in the Earth and Planets. Cambridge Univ. Press, Cambridge, U.K. http://dx.doi.org/10.1017/CBO9780511612879.

Seber, D., Barazangi, M., Ibenbrahim, A., Demnati, A., 1996. Geophysical evidence for lithospheric delamination beneath the Alboran Sea and Rif-Betic Mountains. Nature 379, 785–790.

Stern, T.A., Stratford, W.R., Salmon, M.L., 2006. Subduction evolution and mantle dynamics at a continental margin: Central North Island, New Zealand. Reviews of Geophysics 44, RG4002. http://dx.doi.org/10.1029/2005RG000171.

Stock, G.M., Anderson, R.S., Finkel, R.C., 2005. Rates of erosion and topographic evolution of the Sierra Nevada, California, inferred from cosmogenic ^{26}Al and ^{10}Be concentrations. Earth Surface Processes and Landforms 30, 985–1006. http://dx.doi.org/10.1002/esp.1258.

Tilmann, F., Ni, J., INDEPTH III Seismic Team, 2003. Seismic imaging of the downwelling Indian lithosphere beneath central Tibet. Science 300 (5624), 1424. http://dx.doi.org/10.1126/science.1082777.

Trexler, J., Cashman, P., Cosca, M., 2012. Constraints on the history and topography of the Northeastern Sierra Nevada from a Neogene Sedimentary basin in Reno-Verdi area, Western Nevada. Geosphere 8, 545–561. http://dx.doi.org/10.1130/GES00735.1.

Tritton, D.J., 1988. Physical Fluid Dynamics. Oxford Clarendon Press, Oxford Science Publications (519 pp.).

Valera, J.L., 2009. Development and Application of Numerical Thermomechanical Modeling of Continental Delamination Processes. PhD thesis (in Spanish) Univ. Complutense de Madrid (224 pp.).

Valera, J.L., Negredo, A.M., Villaseñor, A., 2008. Asymmetric delamination and convective removal numerical modeling: comparison with evolutionary models for the Alboran Sea region. Pure and Applied Geophysics 165, 1683–1706. http://dx.doi.org/10.1007/s00024-008-0395-8.

Valera, J.L., Negredo, A.M., Jiménez-Munt, I., 2011. Deep and near-surface consequences of root removal by asymmetric continental delamination. Tectonophysics 502, 257–265. http://dx.doi.org/10.1016/j.tecto.2010.04.002.

Vissers, R.L.M., 2012. Extension in a convergent tectonic setting: a lithospheric view on the Alboran system of SW Europe. Geologica Belgica 15 (1–2), 53–72.

Wallner, H., Schmeling, H., 2010. Rift induced delamination of mantle lithosphere and crustal uplift: a new mechanism for explaining Rwenzori Mountains' extreme elevation? International Journal of Earth Sciences (Geol Rundsch) 99, 1511–1524. http://dx.doi.org/10.1007/s00531-010-0521-6.

Wernicke, B., Clayton, R., Ducea, M., Jones, C., Park, S., Ruppert, S., Saleeby, J., Snow, J., Squires, L., Fliedner, M., Jiracek, G., Keller, R., Klemperer, S., Luetgert, J., Malin, P., Miller, K., Mooney, W., Oliver, H., Phinney, R., 1996. Origin of high mountains in the continents: the Southern Sierra Nevada. Science New Series 271 (5246), 190–193.

West, J.D., Fouch, M.J., Roth, J.B., Elkins-Tanton, L.T., 2009. Vertical mantle flow associated with a lithospheric drip beneath the Great Basin. Nature Geoscience 2, 439–444. http://dx.doi.org/10.1038/NGEO526.

Zandt, G., Gilbert, H., Owens, T.J., Ducea, M., Saleeby, J., Jones, C.H., 2004. Active foundering of a continental arc root beneath the southern Sierra Nevada in California. Nature 431, 41–46.